

# TELAMON: TeV Effelsberg Long Term AGN Monitoring

## Program Description and Sample Characterization

(author list tbc)

1

Received April XX, 2022; accepted Month XX, 2022

### ABSTRACT

**Aims.** We introduce the TELAMON program which is using the Effelsberg 100-m telescope to monitor the radio spectra of active galactic nuclei (AGN) under scrutiny in astroparticle physics, namely TeV blazars and candidate neutrino-associated AGN. Here, we are presenting and characterizing our main sample of TeV-detected blazars.

**Methods.** We present results from the first 2 years, obtained since August 2020. During this pilot phase we have observed all (known to date) TeV-detected blazars in the Northern Hemisphere ( $\text{Dec} > 0^\circ$ ) whose flux density falls below 500 mJy in the low state. The remaining brighter sources are already well covered by other programs. We discuss the basic data reduction and calibration procedures used for all TELAMON data and introduce a sub-band averaging method used to calculate average light curves for the sources in our sample.

**Results.** We find that the TeV-selected sources in our sample exhibit a median flux density of 0.41 Jy at 14 mm. The spectrum for most of the sources is consistent with a flat radio spectrum, we find an average spectral index of  $\alpha = -0.14 \pm 0.19$  with a median of  $\alpha = -0.13$  in our sample. Our results are consistent with previous studies of TeV-selected blazars, but differ significantly e.g. from the GeV-selected F-GAMMA sample. While the spectral indices found in our sample and the GeV-selected F-GAMMA are consistent with each other, our TeV-selected blazar sample mostly consists of fainter radio sources than what F-GAMMA has observed. This is consistent with the idea of the blazar sequence that the double-humped spectrum of blazars is shifted to higher frequencies for TeV-emitters, which results in a lower radio flux density. On top of that, we present a strategy which is well suited to track the light curve evolution of sources in our sample for variability and correlation analysis we are planning for the future.

**Key words.** blazars – TeV – jetted AGN – radio

## 1. Introduction

Blazars are active galactic nuclei (AGN) that emit violently variable broadband emission from radio to  $\gamma$ -ray energies. With decreasing luminosity, the peaks of their characteristic double-humped broadband spectra are shifted upwards and the high-energy emission reaches the very-high-energy (VHE) regime at TeV gamma rays. High-peaked BL Lac objects (HBLs) are canonically defined as sources whose synchrotron emission hump peaks above  $10^{15}$  Hz (Padovani & Giommi 1995). In the most extreme cases, they can reach up even higher by up to two orders of magnitude (Ghisellini 1999; Biteau et al. 2020). Blazars are of utmost interest for astroparticle physics as possibly dominant sources of ultrahigh-energy cosmic rays and neutrinos (Hillas 1984; Mannheim 1995, e.g.,). In particular, HBLs and extreme blazars have been considered in several recent theoretical works as relevant neutrino sources (Tavecchio et al. 2014; Padovani et al. 2015; Giommi et al. 2020). Here, we present the first results of our newly setup TELAMON (TeV Effelsberg Long-term AGN Monitoring) program. We are performing radio monitoring observations of a sample of TeV-selected blazars at high frequencies up to 44 GHz to trace dynamical process in this objects. This program is designed to monitor the radio spectra of AGN, namely TeV-blazars and candidate neutrino AGN with the Effelsberg telescope since August 2020. A first study of TeV-selected HBL and Extreme Blazars has been presented by Lindfors et al. (2016) at 15 GHz, we extend their observations with radio coverage at multiple frequencies, and for the

first time spectral characterization of these objects. In Section 2 we explain in detail the sample selection and observing setup used with the Effelsberg 100-m telescope. On top of that we present our TELAMON analysis pipeline including cross-scan setup and calibration procedures. In Section 3, we present the first results for sources in our sample and present average flux densities and spectral indices for all observed sources. These results are discussed and compared with previous studies, e.g. the Lindfors et al. (2016) study in Section 4. Moreover, we compare source properties of the TeV-selected sources in our sample with the GeV-selected F-GAMMA (Fuhrmann et al. 2016; Angelakis et al. 2019) sample and discuss similarities and differences.

## 2. Observations & Analysis

### 2.1. Program Description & Sample

The main TELAMON sample consists of TeV-detected and neutrino-candidate AGN, excluding bright low-peaked blazars, which are well covered in other monitoring programs. As a selection criterion, all sources whose low-state flux density falls below 500 mJy are included. The complete sample, consisting of 44 sources is presented in Table 1. It consists of 18 XBLs (i.e.,  $\nu_{\text{peak}} > 10^{17}$  Hz, and sources from Biteau et al. 2020), 12 HBLs (i.e.,  $10^{15}$  Hz  $< \nu_{\text{peak}} < 10^{17}$  Hz), 6 FSRQs, 5 IBLs, 1 LBL and 1 Radio Galaxy (RG). J0509+0541 (TXS 0506+056) is included in the HBL count due to its high peak frequency found in the literature. For J0316+4119 (IC 310), a clear characteri-

zation is not yet possible since the source shows some Blazar-like properties but its jet might be misaligned by  $10\text{--}20^\circ$  from the line of sight (Ahnen et al. 2017). The prime research subject of the TELAMON program are HBLs and XBLs, other sources are included to allow for statistical comparison. Every two to four weeks, high-cadence observations of these sources are performed at multiple high radio frequencies up to  $\nu = 44$  GHz.

## 2.2. Observations

For our observations we are using the Effelsberg 100-m telescope operated by the Max-Planck-Institute for Radio Astronomy in Bonn, Germany. The observations are conducted with 20 mm, 14 mm and 7 mm receivers in continuum observing mode with the backend dual-spec-OPTOCBE. This results in four sub-bands (centered at 19.25 GHz, 21.15 GHz, 22.85 GHz and 24.75 GHz) for the 14 mm receiver and four sub-bands (centered at 36.25 GHz, 38.75 GHz, 41.25 GHz, 43.75 GHz) for the 7 mm receiver. Since spring 2021, the 20 mm receiver has been added yielding two additional frequency bands (centered at 14.25 GHz and 16.75 GHz). All receivers are equipped with two horns. The first horn is pointed directly at the target and passes the signal directly to the receiver. The second horn is pointed at the atmosphere off-source and is used to subtract weather effects from the first horn. This is important, because at the observed frequencies Earth's atmosphere (especially on cloudy days) emits thermal radiation that needs to be accounted for. In order to measure the flux densities of the sources, cross-scans are performed on the targets, consisting of typically 8 sub-scans at 20 mm, 14 mm and 7 mm (36.25 GHz, 38.75 GHz). For the higher 7 mm frequencies (41.25 GHz, 43.75 GHz) 16 sub-scans are used. A cross-scan means that the telescope hovers over the point-like source region in azimuth- and elevation-direction multiple times while measuring the antenna temperature of the receiver. About every four hours, a calibrator source is observed in order to focus the telescope and to extract calibration factors (see Sect. 2.4). This setup is well suited to trace dynamical processes in the compact parsec-scale jets of blazars related to high-energy flares or neutrino detections.

For this work we consider all observations from within the first 1.5 years of the program from August 2020 to February 2022. This comprises data taken in 60 observing sessions with a total observing time of 648.2 hours. During this time we have observed 55 distinct sources in total, 49 at 20mm, 51 at 14mm and 37 at 7mm. Note that part of the observing time was also used for observations of Neutrino-candidate sources, which will be discussed in a separate publication.

## 2.3. Data Reduction

The general data analysis for pointed flux density measurements with the Effelsberg 100-m telescope has been described in detail by Angelakis et al. (2019) in context of the F-GAMMA program. We use a very similar data reduction procedure and will therefore restrict this section on the changes and improvements compared to the analysis of Angelakis et al. (2019). The major improvements presented here are a semi-automated flagging algorithm, a new calibration procedure and an in-depth error discussion. In principle, this section deals with how the raw data output of every scan, namely radiation temperatures, is converted into astrophysical units of Jansky.

### 2.3.1. Subscan Fitting

As mentioned in Sect. 2.2, every scan of a source at a specific frequency consists of multiple sub-scans. These multiple sub-scans are used to calculate one flux density value for each frequency per scan. First of all, for every scan, all azimuth sub-scans are used to generate a single average azimuth scan and all elevation sub-scans are used to generate a single average elevation scan. Since all of the sample sources are assumed to be point-like, a Gauss curve is fitted to both average scans. At this point, it is important to perform a data quality check, to see if all sub-scans can be considered good scans. This is important, since some sub-scans might be damaged due to radio frequency interference (RFI), telescope errors or atmospheric effects, and therefore might lead to errors in the flux density values.

In order to filter out bad sub-scans, a flagging system has been developed, that uses multiple criteria to detect bad scans. A scan is flagged if at least one of the following criteria applies:

- The full-width at half maximum (FWHM) of the Gauss fit of either the azimuth or elevation or both average scans deviates by more than 30% from the HPBW (depending on the frequency). *Reason: The FWHM of a point-source scan is restricted by the angular resolution limit (beam width), depending on the observing frequency. Therefore, it should stay constant for each frequency and not vary too much from source to source. There can be small positional telescope uncertainties throughout the sub-scans that lead to a slightly different FWHM of the averaged source scan, but these changes should not exceed  $\sim 30\%$ . This flag type is typical for windy observing sessions, where the telescope's position changes slightly from sub-scan to sub-scan by wind gusts, or in cases where the source is below the detection limit and atmospheric background is fitted.*
- The Gaussian fit of either azimuth or elevation or both average scans has negative amplitude. *Reason: The sources are expected to be point-like radio emitters, this means one expects to observe a Gauss signal with peak. Since a negative amplitude indicates a dip in the Gaussian, there is something wrong with one or more sub-scans. It can also indicate that the source is below the detection limit and not visible at all, i.e., only background noise is fitted.*
- The maximum of the Gauss fit of either azimuth or elevation or both average scans has an offset from the scan center greater than 20% of the HPBW. *Reason: The Gauss fit is expected to be centered in azimuth and elevation scans. If this is not the case, the cross scan has missed the source center by several arcseconds. In principle, these cases are corrected in the analysis (see Sect. 2.3.2), but at a level of more than 20% of the beam width this offset correction is not accurate anymore.*
- The amplitudes of the Gauss fits of azimuth and elevation average scans differ by more than 15%. *Reason: The source is expected to be point-like and centered in azimuth and elevation scans. This means the average scans in azimuth and elevation should have similar amplitudes. If amplitudes differ by more than 15% this is an indication of bad underlying sub-scans included in the average scan.*

Note that the exact limits that indicate when a scan is flagged rely on experience. The chosen values have proven to be well suited for the analysis in the used frequency bands. If an averaged scan is flagged according to these criteria, it is not trivial to judge whether the source was below the detection limit (not visible in all sub-scans) or if there were simply a few bad sub-scans

**Table 1.** The TELAMON sample of TeV-emitting and neutrino-candidate AGN. The classification into XBL, HBL, IBL and LBL is performed according to the synchrotron peak frequency found in the literature. The presented references are related to the synchrotron peak frequency and the redshift value.

| ID<br>(J2000) | Alternative<br>Name   | Class   | Synchr. Peak<br>$\text{Log}_{10}\left(\frac{\nu_{\text{peak}}}{\text{Hz}}\right)$ | Redshift <sup>a</sup> | Reference <sup>b</sup> | Sample |
|---------------|-----------------------|---------|-----------------------------------------------------------------------------------|-----------------------|------------------------|--------|
| J0035+5950    | IES 0033+595          | XBL     | 18.2                                                                              | 0.086                 | [1]                    | -      |
| J0112+2244    | S2 0109+22            | IBL     | ~ 15                                                                              | 0.4                   | [2]                    | II     |
| J0136+3906    | RGB J0136+391         |         |                                                                                   |                       |                        | -      |
| J0152+0146    | RGB J0152+017         |         |                                                                                   |                       |                        | -      |
| J0214+5144    | TXS 0210+515          | XBL     | 17.3                                                                              | 0.049                 | [1]                    | I      |
| J0221+3556    | S3 0218+35            | FSRQ    | -                                                                                 | 0.954                 | [3]                    | II     |
| J0222+4302    | 3C 66A                | HBL     | 15.63                                                                             | 0.34                  | [4]                    | II     |
| J0232+2017    | IES 0229+200          | XBL     | 18.5                                                                              | 0.139                 | [1]                    | -      |
| J0303-2407    | PKS 0301-243          | HBL     | 15.7                                                                              | 0.266                 | [1]                    | I      |
| J0316+4119    | IC 310                | RG/XBL  | 17                                                                                | 0.0189                | [6]                    | I      |
| J0319+1845    | RBS 0413              |         |                                                                                   |                       |                        | -      |
| J0416+0105    | IES 0414+009          | XBL     | 16.5                                                                              | 0.287                 | [1]                    | -      |
| J0507+6737    | IES 0502+675          | XBL     | 17.9                                                                              | 0.34                  | [1]                    | -      |
| J0509+0541    | TXS 0506+056          | IBL/HBL | 15.34                                                                             | 0.3365                | [4]                    | II     |
| J0521+2112    | RGB J0521+212         | IBL     | 15.1                                                                              | 0.108                 | [1]                    | II     |
| J0648+1516    |                       |         |                                                                                   |                       |                        | -      |
| J0650+2502    | IES 0647+250          | HBL     | 16.7                                                                              | 0.203                 | [1]                    | I      |
| J0710+5909    | RGB J0710+591         | XBL     | 18.1                                                                              | 0.12                  | [1]                    | -      |
| J0733+5153    | PGC 2402248           | XBL     | 17.9                                                                              | 0.09                  | [1]                    | -      |
| J0809+5219    | IES 0806+524          |         |                                                                                   |                       |                        | I      |
| J0812+0237    | 1RXS J081201.8+023735 |         |                                                                                   |                       |                        | -      |
| J0847+1135    | RBS 0723              | XBL     | 17.8                                                                              | 0.198                 | [1]                    | -      |
| J0913-2103    | MRC 0910-208          | XBL     | 17.1                                                                              | 0.198                 | [1]                    | I      |
| J1015+4926    | IES 1011+496          | HBL     | 16.4                                                                              | 0.2                   | [1]                    | I      |
| J1058+2817    | GB6 J1058+2817        | XBL     | 18.37                                                                             | 0.4793                | [4]                    | I      |
| J1104+3812    | Mrk 421               | XBL     | 16.3                                                                              | 0.03                  | [1]                    | II     |
| J1136+7009    | Mrk 180               | HBL     | 16.8                                                                              | 0.045                 | [1]                    | I      |
| J1136+6737    | RX J1136.5+6737       | XBL     | 18.1                                                                              | 0.134                 | [1]                    | -      |
| J1145+1936    | 3C 264                | RG      | -                                                                                 | 0.0216                | [5]                    | I      |
| J1217+3007    | ON 325                | HBL     | 15.58                                                                             | 0.131                 | [4]                    | II     |
| J1221+3010    | IES 1218+304          | XBL     | 16.8                                                                              | 0.18                  | [1]                    | -      |
| J1221+2813    | W Comae               | IBL     | 14.84                                                                             | 0.102                 | [4]                    | II     |
| J1224+2436    | MS 1221.8+2452        |         |                                                                                   |                       |                        | -      |
| J1230+2518    | ON 246                | IBL     | 15.0                                                                              | 0.135                 | [1]                    | II     |
| J1415+1320    | PKS 1413+135          |         |                                                                                   |                       |                        | II     |
| J1422+3223    | OQ 334                | FSRQ    | -                                                                                 | 0.681                 | [8]                    | II     |
| J1427+2348    | OQ 240                | HBL     | 15.7                                                                              | 0.647                 | [4]                    | II     |
| J1428+4240    | IES 1426+428          | XBL     | 18.1                                                                              | 0.129                 | [1]                    | -      |
| J1443+1200    | IES 1440+122          | XBL     | 17.7                                                                              | 0.16                  | [1]                    | -      |
| J1443+2501    | PKS 1441+25           | FSRQ    | -                                                                                 | 0.939                 | [9]                    | I      |
| J1518-2731    | TXS 1515-273          | HBL     | 15.3                                                                              | 0.14                  | [1]                    | I      |
| J1555+1111    | PG 1553+113           | HBL     | 15.6                                                                              | 0.36                  | [1]                    | I      |
| J1653+3945    | Mrk 501               | XBL     | 17.9                                                                              | 0.03                  | [1]                    | II     |
| J1725+1152    | H 1722+119            |         |                                                                                   |                       |                        | I      |
| J1728+5013    | IZw 187               | XBL     | 17.0                                                                              | 0.055                 | [1]                    | I      |
| J1743+1935    | IES 1741+196          | XBL     | 17.8                                                                              | 0.08                  | [1]                    | I      |
| J1813+3144    | B2 1811+31            | FSRQ    | 15.0                                                                              | 0.117                 | [1]                    | I      |
| J1943+2118    | HESS J1943+213        |         |                                                                                   |                       |                        | -      |
| J1958-3011    | 1RXS J195815.6-301119 | XBL     | 17.0                                                                              | 0.119                 | [1]                    | I      |
| J1959+6508    | IES 1959+650          | XBL     | 16.9                                                                              | 0.047                 | [1]                    | I      |
| J2001+4352    | MAGIC J2001+435       |         |                                                                                   |                       |                        | I      |
| J2039+5219    | IES 2037+521          |         |                                                                                   |                       |                        | -      |
| J2158-3013    | PKS 2155-304          | HBL     | 15.4                                                                              | 0.117                 | [1]                    | I      |
| J2250+3825    | B3 2247+381           |         |                                                                                   |                       |                        | -      |
| J2243+2021    | RGB J2243+203         | XBL     | 15.1                                                                              | -                     | [1]                    | I      |
| J2347+5142    | IES 2344+514          | XBL     | 17.7                                                                              | 0.044                 | [1]                    | I      |

<sup>a</sup> For some sources, no redshift was found in the given reference. In these cases, if available, the redshift value was taken from either SIMBAD (<http://simbad.u-strasbg.fr/simbad/>) or NED (<https://ned.ipac.caltech.edu/>). For a couple of sources, the redshift is still undetermined. <sup>b</sup> Reference for redshift and peak frequency: [1] Chang et al. (2019), [2] Ciprini et al. (2004), [3] Paiano et al. (2017), [4] Nieppola et al. (2006), [5] Ahn et al. (2012), [6] Ahnen et al. (2017), [7] Sowards-Emmerd et al. (2005), [8] Abazajian et al. (2009), [9] Shaw et al. (2012), [10] Shaw et al. (2013), [11] Ackermann et al. (2015)

| Receiver         | $A_0$ | $A_1$     | $A_2$     |
|------------------|-------|-----------|-----------|
| 20 mm            | 0.971 | 1.833E-3  | -2.867E-5 |
| 14 mm            | 0.962 | -1.950E-3 | -2.493E-5 |
| 7 mm (36-39 GHz) | 0.835 | 8.312E-3  | -1.046E-4 |
| 7 mm (41-44 GHz) | 0.785 | 1.126E-2  | -1.475E-4 |

**Table 2.** Gain curve parameters used for the different receivers of the Effelsberg 100-m telescope

by not looking at the individual sub-scans for every source. As done by Angelakis et al. (2019) a manual analysis of individual sub-scans is possible but very tedious, time-consuming, and also not clearly reproducible since it depends on the analyzer’s individual eyes. Therefore, a semi-automated analysis tool has been developed which takes care of detecting and sorting-out bad sub-scans.

For every scan (usually consisting of 8 or 16 sub-scans), it is first checked if the averaged scan is flagged. If the scan is not flagged, it will be used as-is for the next analysis steps without performing any changes. If the scan is flagged, the algorithm tries to remove one (arbitrary) sub-scan and checks if the average scan (excluding the removed sub-scan) is still flagged. If this new average scan is not flagged, the average scan, excluding the deleted scan, will be used for further analysis steps. If the new average scan is still flagged this procedure goes on until the algorithm has found a combination of removed sub-scans that leads to a non-flagged average scan. To be conservative, the algorithm allows for only one sub-scan in total to be removed from the initial scan. If the average scan is still flagged after trying to remove all sub-scan combinations, the scan is sorted out as a bad scan and it is not used for further analysis. The automated analysis quality is superior to the manual analysis since every sub-scan deletion can be tried out, instead of simply judging by the human eye what sub-scan deletion might improve the overall fit quality. On top of that, due to the appointed flagging criteria, it is completely reproducible. As a final check, the data are again inspected manually to sort out any outliers and left-over bad scans that the algorithm was not able to detect.

### 2.3.2. Data Corrections

All averaged scans that were not sorted out by our semi-automated flagging algorithm undergo further data reduction processes. This data reduction process is equivalent to the pointing offset correction, atmospheric opacity correction and elevation-dependent gain correction presented by Angelakis et al. (2019) in their chapter 4. The only difference is that we determine the zenith opacity  $\tau$  using a water-vapor radiometer near the telescope by measuring the strength of the 22 GHz water-vapor line. On top of that, we use updated gain curve parameters  $A_i$  as presented in Table 2.

## 2.4. Calibration

### 2.4.1. Calibrator Sources

In this section, it is discussed how the calibration factor for the analysis is determined. Baars et al. (1977) have introduced a set of secondary calibrators that can be used on a day-to-day basis for calibration purposes. Their flux density is very constant over long periods of time (several decades) and they are also very compact sources. These secondary calibrators have been further investigated and monitored by Ott et al. (1994) and most lately

by Perley & Butler (2013, 2017). According to the latest publication (Perley & Butler 2017), the best suited calibrators in the TELAMON frequency range (19 GHz–44 GHz) are 3C 286 and 3C 295. They are therefore used as calibrator sources in this work. Perley & Butler (2017) provide parametrized spectra for these sources, that are used to calculate the frequency dependent calibrator flux densities for this thesis. Since 3C 295 is quite faint ( $\lesssim 1$  Jy) at higher frequencies ( $\nu \gtrsim 35$  GHz) and therefore not always detectable (especially during bad weather sessions), the sources NGC 7027 and W3(OH) are also included as calibrator sources. NGC 7027 is a planetary nebula and has been proposed as a secondary calibrator by Baars et al. (1977) but has later been found to be variable. Still, this source can be used as a calibrator, since its variability has been well characterized by Zijlstra et al. (2008). The spectral model provided in this paper is used to calculate time-dependent calibration flux densities for NGC 7027. W3(OH) is a star forming region that exhibits a strong water maser in the 14 mm band (Hachisuka et al. 2006). Therefore, it is excluded for 14 mm calibration, but since the source is very bright at 7 mm ( $\approx 3$  Jy) it is useful as a substitute for 3C 295 in this band. For W3(OH) we use our own calibration model which was created using Effelsberg archival data and assuming a free-free emission model. Due to their brightness, the two main calibrators observed with highest priority are 3C 286 and NGC 7027. 3C 295 is used as a backup calibrator at 14 mm and W3(OH) as a backup calibrator at 7 mm.

### 2.4.2. Calibration Process

As mentioned in Sect. 2.2, usually one of the secondary calibrator sources are observed every four hours during an observing session to determine the calibration factor. This calibration measurement typically consists of up to three scans per frequency on the calibrator. If there was more than one scan on the calibrator at the same time, the mean and standard deviation are calculated to get a value with error for the total calibration factor at any given time. In the special case of only one calibrator measurement the error is estimated, depending on the frequency (see Sect. 2.5). For each observing session, one therefore gets a calibration factor for every  $\sim 4$  hours, in the ideal case. In a lot of epochs, especially during the beginning of the program, there are less calibration measurements, due to a still inexperienced observer team. An example is given in Fig. 1, where all calibration factor data points (blue) are averages of the underlying (multiple) calibrator scans at the time. When talking about calibration factors in the following, it is referred to these, already (sub-)averaged calibration factors like the (blue) ones presented in Fig. 1.

In principle, the calibration factor only depends on the telescope’s sensitivity at a given frequency and should therefore be constant throughout an observing session (for a given frequency). As one can see in Fig. 1 this is not always the case. The calibration factor does change throughout the observing session, mostly due to temperature changes which affect the ideal focus position. If the telescope is out of focus, the received signal is weaker and therefore the calibration factor rises. The telescope is being kept in focus by readjusting the focus every four hours (or more often in the case of significant temperature drops) to keep the calibration factor constant, but still the calibration factor varies throughout the observation. The de-focusing of the telescope also turns out to be a major issue in early epochs due to the limited number of calibration and focus scans performed by the still inexperienced observer team. Modelling the behaviour of the focus is non-trivial, since it is unknown how much of the

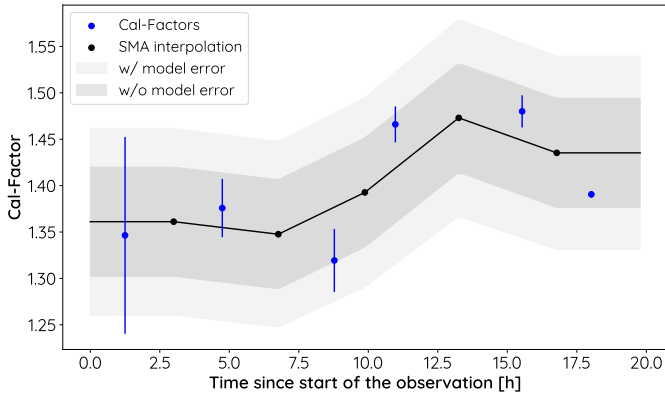


**Fig. 1.** Exemplary calibration factor evolution at 38.75 GHz during the observing session on Oct 24, 2021. The blue data points correspond to the (sub-)averaged calibration factor measurements  $\Gamma_{c,i}$ . The black line indicates the SMA-interpolated calibration factor  $\Gamma_{\text{SMA},i}$  (see Equation (1)), as used in the final analysis. The dark gray area represents the calibrator scatter  $\sigma_{\text{sc},v}$ , while the light gray area represents the total calibration uncertainty  $\sigma_{\text{cal}}$ , including the model error  $\sigma_{\text{model}}$  and  $\sigma_{\text{sc},v}$ .

calibration factor fluctuation is statistical and how much is systematic due to, e.g., shifting focus. If the fluctuation was solely statistical, one would have to take the mean calibration factor throughout the entire session. If the fluctuation was solely systematic it would be best to linearly interpolate between the calibration factors. In the present case, however, interpolation between all data points would be an over-interpretation of the data and taking the mean cannot account for the fluctuation of the calibration factor. In order to take this fluctuation into account and also not to over-interpret the data points, the calibration factor is modelled using a simple moving average (SMA) interpolation (Chou 1975). This is essentially a combination of both methods, since first, the mean between two adjacent calibration factor values is taken and then it is interpolated between these mean values. If the calibration factor at time  $t_i$  is  $\Gamma_{c,i}$ , the interpolated values are calculated following

$$\Gamma_{\text{SMA},i} = \frac{\Gamma_{c,i} + \Gamma_{c,i+1}}{2}, \quad (1)$$

where  $\Gamma_{c,i+1}$  is the calibration factor adjacent to  $\Gamma_{c,i}$ . The same procedure is used for the time interpolation

$$t_{\text{SMA},i} = \frac{t_i + t_{i+1}}{2}. \quad (2)$$

If initially there are  $n$  calibration factors  $\Gamma_{c,i}$ , this interpolation will result in  $n - 1$  interpolated calibration factors  $\Gamma_{\text{SMA},i}$ . As indicated by the black line in Fig. 1, it is interpolated linearly between the  $(t_{\text{SMA},i}, \Gamma_{\text{SMA},i})$  values to get a general expression for the calibration factor, at any given time. For times  $t < t_{\text{SMA},1}$ , the calibration factor is modelled as constant  $\Gamma_{\text{SMA},1}$ . Analogously, for times  $t > t_{\text{SMA},n-1}$ , the calibration factor is modelled as constant  $\Gamma_{\text{SMA},n-1}$ . If there is only one or two calibration factors available ( $n = 1, 2$ ), a constant calibration factor is assumed for the entire epoch. The interpolation (black line) is used to determine the calibration factor at any given time during the observing session. This means, for every source scan, one calculates the corresponding calibration factor  $\Gamma_c$  using the SMA-interpolation and then uses this calibration factor to calculate the flux density of the source  $S_{\text{source}}$  following:

$$S_{\text{source}} = T_{\text{src}} \cdot \Gamma_c. \quad (3)$$

## 2.5. Error Discussion

In this section, the determination of the total flux density uncertainties  $\sigma_{\text{tot}}$  is discussed. The final error has to include the main errors due to the sub-scan-fitting process with the data corrections,  $\sigma_{\text{fit}}$ , and the uncertainty of the calibration factor,  $\sigma_{\text{cal}}$ .

Let us first discuss the uncertainty due to sub-scan fitting and data corrections,  $\sigma_{\text{fit}}$ . This error is calculated through Gaussian error propagation from the fitting and data correction process explained in Sect. 2.3.2. Note that the gain curve is assumed to be free of error here, since the accuracy of the gain curve is also reflected in the fluctuation of the calibration factors and therefore included in the calibration error  $\sigma_{\text{cal}}$ . Usually, atmospheric corrections have the biggest impact on the data correction error, especially during bad weather sessions. In total,  $\sigma_{\text{fit}}$  is on average of the order  $\sim 1\%$ .

The main contribution of the flux density uncertainties comes from the calibration error,  $\sigma_{\text{cal}}$ . There are two sources of error that determine the total calibration error. First, one needs to consider the fluctuation of the calibration factor  $\sigma_{\text{sc},v}$  for each frequency and observing epoch. Secondly, one needs to account for the uncertainty of the underlying calibrator model  $\sigma_{\text{model}}$ . Let us first discuss how  $\sigma_{\text{sc},v}$  is determined. As explained in the previous section, an SMA-interpolation is used to calculate interpolated calibration factors. To be conservative, the error of the interpolated calibration factors is assumed to be constant. Therefore, the standard deviation of all (non-interpolated) calibration factors for each frequency and observing epoch is used as the error

$$\sigma_{\text{sc},v} = \sqrt{\frac{1}{n-1} \sum_{i=1}^n (\Gamma_{c,i} - \bar{\Gamma}_c)^2}, \quad (4)$$

here  $\bar{\Gamma}_c$  is the mean over the non-interpolated calibration factors  $\Gamma_{c,i}$ . This error is also illustrated in Fig. 1 by the gray background. In the special case where only one calibration factor was measured during an observing epoch, it is non-trivial to determine a sensible value for this error. In order to deal with this special case, the calibration factor scattering for each frequency from all observing epochs has been analyzed. An exemplary plot of the calibration factor evolution at 41.25 GHz throughout the entire program since August 2020 is shown in Fig. 2. In order to derive a sensible error for these epochs, the standard deviation of all calibration factors throughout the program is used to get an estimate of the average calibration factor scatter. This analysis is performed for every frequency band. As a conservative estimate, a calibration error of 5% is used at 20 mm and 14 mm and 10% at 7 mm for epochs with only one calibration factor. In Fig. 2, one can also see that for some epochs the calibration factor varies more than for others. This is due to focusing problems mainly during early observing sessions, shortly after the beginning of the program. During the early epochs the 4 hour calibration rhythm was not always kept and less calibration/focus measurements were performed. Therefore, most of the epochs where only one calibration measurement was made are during the first months.

On top of the calibration factor scattering  $\sigma_{\text{sc},v}$ , one also needs to take into account the accuracy of the calibrator models  $\sigma_{\text{model}}$ . The models of 3C 295 and 3C 286 by Perley & Butler (2017) have an estimated accuracy of 3% to 5%, with the larger errors at the lowest ( $\sim 50$  MHz) and highest ( $\sim 50$  GHz) ends. Since the observations take place from 19 GHz–44 GHz, which is at the higher end of their scale, an error of 5% for the 3C 295 and 3C 286 models is assumed. For the timely variable model

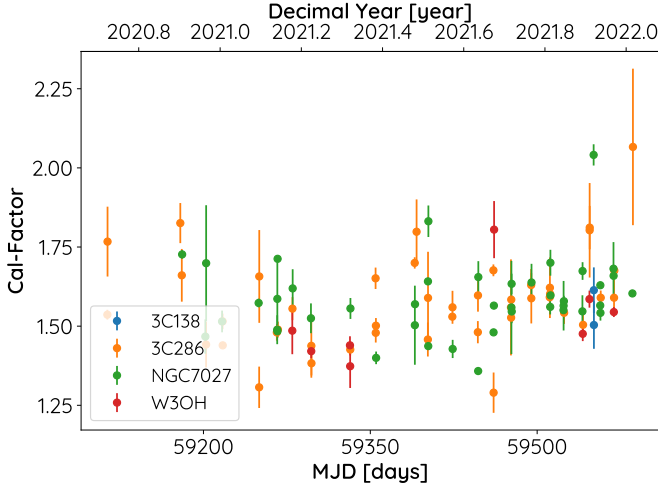


**Fig. 2.** Exemplary calibration factor evolution at 41.25 GHz throughout the entire program. We determine the calibration factor scattering error  $\sigma_{sc,v}$  by taking the standard deviation of these values at each frequency throughout the program.

of NGC 7027, Zijlstra et al. (2008) provide an uncertainty of 6 %. It is estimated that the uncertainty for the W3(OH) model is also in the same range, since it has a similar underlying free-free emission model. As a conservative estimate, a general accuracy of the calibrator models of  $\sigma_{model}/\Gamma_c = 6\%$  is assumed, which is the maximum error out of the models. One must not use the Gaussian law of error propagation to combine the uncertainties of the different models, since they are not statistically independent and all based on the same flux density scale by Baars et al. (1977). To calculate the total calibration uncertainty  $\sigma_{cal}$ , Gauss addition is performed of the estimated model error  $\sigma_{model}$  and the calibration scatter  $\sigma_{sc,v}$ , which is individual for every epoch and frequency, as described above. The total calibration error is therefore given by

$$\sigma_{cal} = \sqrt{\sigma_{model}^2 + \sigma_{sc,v}^2}. \quad (5)$$

In order to obtain the total flux density error  $\sigma_{tot}$ , one needs to combine  $\sigma_{cal}$  with the fitting error  $\sigma_{fit}$ . This is done by Gaussian error propagation. Following Equation (3), one finds

$$\frac{\sigma_{tot}}{S_{source}} = \sqrt{\left(\frac{\sigma_{cal}}{\Gamma_c}\right)^2 + \left(\frac{\sigma_{fit}}{T_{src}}\right)^2} \quad (6)$$

for the total flux density error. Note that for the following analysis the model error is considered to be zero, since it is purely systematic throughout the entire program. Using it would therefore lead to an overestimation of the statistical flux density error. If the presented flux density values would be combined with other radio data (using a different flux density scale), or if the absolute flux density values are of interest, the model error has to be taken into account.

## 3. Results

### 3.1. Average Spectral Indices

In order to characterize the TELAMON sample in terms of the spectral index, we calculate a spectral index for every source, averaged over all individual spectra observed during different

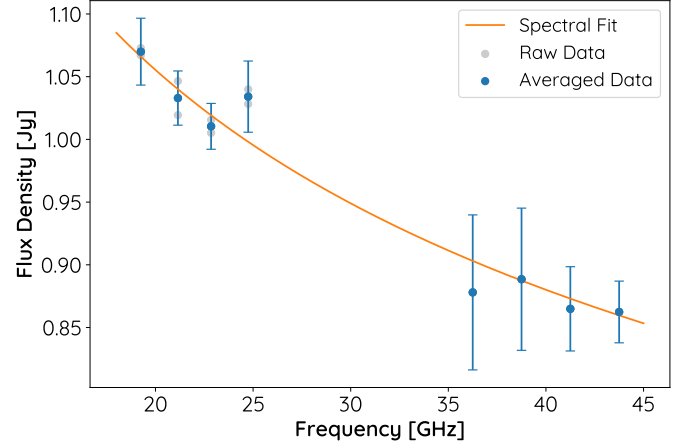


**Fig. 3.** Example of the spectral fitting process (Mrk 501 on July 28, 2021). The light gray dots indicate the raw data, errors are not shown to enhance readability. For every frequency, where more than one raw flux density value is available, the flux densities are averaged (blue dots). The averaged flux densities are then fitted with a power-law spectrum. In the presented case, one finds  $\alpha = -0.262 \pm 0.021$ .

epochs. To ensure comparability, the spectral index has only been calculated within the 14 mm band, since sufficient 14 mm coverage is available for almost all sources (48 sources).

#### 3.1.1. Spectral Index Calculation

The calibrated data of the 14 mm receiver consist of flux density values for the frequency sub-bands 19.25 GHz, 21.15 GHz, 22.85 GHz and 24.75 GHz. An example of a calibrated source measurement at these frequencies is shown in Fig. 3. As established earlier, sometimes, there are two detections of a source per epoch, which means that there is more than one flux density value for the same frequency. This can be seen in the example presented in Fig. 3 (gray dots). In this case, the average flux density per frequency is calculated by taking the mean. If there is only one flux density value per frequency available, it is used as-is. The averaged values are depicted as blue dots in Fig. 3. The error is determined by Gaussian error propagation, since distinct scans are considered independent measurements. After this first averaging process, a spectral power-law fit is performed to the data for every source at every observed epoch. This is done for all sources where at least three distinct sub-frequencies were detected within the 14 mm band. The fit is performed using a Levenberg-Marquardt fitting algorithm (Moré 1978). Since the spectrum is expected to be flat ( $\alpha \sim 0$ ), the spectral index is bounded to  $|\alpha| < 1$ . All spectral indices reaching the boundary are excluded from further analysis since this is an indication of outliers in the data. An exemplary fit of Mrk 501 on July 28, 2021 is presented in Fig. 3, which results in a spectral index  $\alpha = -0.262 \pm 0.021$ . This analysis is applied to the entire data set, wherever 14 mm with at least three sub-band detections is available for the same epoch and source. For every source, all spectral indices are then averaged over time to get an expression for the average spectral index of a source. The uncertainty is determined by the standard deviation of the averaged spectral indices. In the special case where only one spectral measurement is available for a source, the fit error is used.



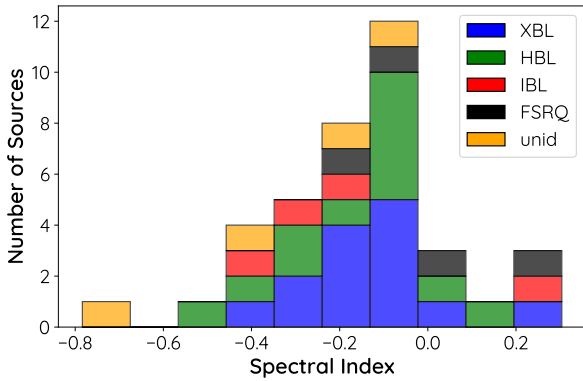


**Fig. 4.** Distribution of the average spectral index across the 14 mm band as found in the TELAMON sample sources.

### 3.1.2. Spectral Indices in the TELAMON sample

All average spectral indices are presented in Table 3, and in Fig. 4 as a histogram plot with bins according to the source type. We find an overall average spectral index of  $-0.16$ , with a standard deviation of  $0.22$  and a median of  $-0.13$ . This is consistent with the expectation of a flat spectrum. The source with the by far steepest spectrum is J1145+1936 ( $\alpha = -0.78 \pm 0.16$ ). Since this is the only source in our sample that is not classified as a blazar but as a radio galaxy, the steep spectrum is also in line with expectations. We therefore conclude that the TeV-selected sub-sample of blazars presented here does not show any unexpected or special spectral features. If we exclude J1145+1936 from the average spectral index calculation we find an average spectral index of  $-0.14$  with standard deviation of  $0.19$  and a median of  $-0.13$ . In order to test if the spectral index distribution of HBL and XBL is statistically different, we perform a two-sample KS-test which leads to a p-value of  $p = 0.96$ . This clearly indicates that the distributions cannot be distinguished and most likely have the same underlying statistics. For all other source classes, the sample size is not sufficient ( $n < 5$ ) to perform significant statistical studies.

### 3.2. Average Flux Densities

In order to simplify the analysis, the observed flux densities of every source and epoch are averaged over the sub-frequencies of the 20 mm, 14 mm and 7 mm receivers. This means for every source we will get an average flux density value at 20 mm, 14 mm and 7 mm for each epoch, given that the source was observed and the detected in these bands. The main reason for this is that in some cases, not all of the four (two for 20 mm) sub-bands of each receiver show a significant source detection. This can be due to RFI, because the source is too weak at the highest frequencies, or due to background noise and receiver malfunction. Averaging over the sub-bands of each receiver will make it possible to compare all epochs with each other, even if a sub-band flux density value might be vacant in one or more epochs. However, taking the mean or the weighted mean of all measured values does not suffice to ensure the comparability of epochs. If, e.g., a source was detected at 19.25 GHz and 21.15 GHz at Epoch A and at another Epoch B at 22.85 GHz and 24.75 GHz, taking the mean will shift the mean frequency of this average. Since the spectrum of the sample sources is in general not always flat ( $S(\nu) \neq \text{const.}$ ), this could turn out to be problematic when

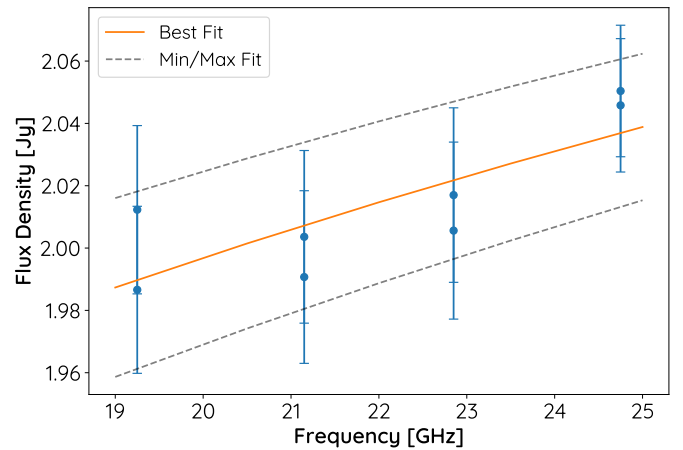


**Fig. 5.** Example of the sub-band averaging process (TXS 0506+056 on Jan 2, 2021 at 14 mm). The average flux density is calculated by taking the integral of the best fit between 19 GHz and 25 GHz. The errors are determined by integrating the Min/Max fits.

comparing flux densities from two distinct epochs. We therefore introduce a new method of obtaining average flux densities from the receiver sub-bands using spectral fits in the following section.

#### 3.2.1. Sub-band Averaging

For each receiver (7 mm, 14 mm and 20 mm), at first a power-law spectral fit  $S(\nu) \propto \nu^\alpha$  is performed to the raw data within the receiver band width. Similar to the spectral index calculation in Sect. 3.1.1, a Levenberg-Marquart fitting algorithm is used to calculate the fit with the spectral index bounded to  $|\alpha| < 0.5$ . Note that here, the bound on  $\alpha$  is even more conservative than for the spectral index calculation, since the analysis presented here is more sensitive to outliers. From the fit, the average flux density  $\bar{S}$  in the range of the receiver bandwidth is calculated:

$$\bar{S} = \frac{\int_{\nu_1}^{\nu_2} S(\nu) d\nu}{\nu_2 - \nu_1}. \quad (7)$$

For the 20 mm receiver the integration limits are  $\nu_1 = 14$  GHz and  $\nu_2 = 17$  GHz, for the 14 mm receiver,  $\nu_1 = 19$  GHz and  $\nu_2 = 25$  GHz, and for the 7 mm receiver  $\nu_1 = 36$  GHz and  $\nu_2 = 44$  GHz. This method ensures that the average flux density is always calculated from the same frequency range, with best knowledge about the intrinsic spectrum of the source for each epoch. In the special case where only data for one sub-frequency (e.g., only for 19.25 GHz) are available, it is not possible to perform a sensible fit. In these cases, a flat spectrum ( $\alpha = 0$ ) is assumed, since this is typical for the sources in the sample.

In order to define an error for the average flux density values, different approaches are used according to how many sub-bands are detected. In the case of two, three or four (i.e., all) sub-frequencies detected, two additional (error-)fits are performed. One with the errors subtracted from the measured flux density values and the other one with the errors added to the measured values. This is justified since in this case, the error mostly consists of systematic calibration uncertainty, i.e., the measured values may all together be higher (or lower) than the best values but relative to each other, they are known much more precisely. This procedure is illustrated in Fig. 5. The error is determined by the difference between min/max-fit and best fit. In the case of

**Table 3.** Average Flux Densities for all sources from the TELAMON sample as observed during the first 1.5 years of the program. The average spectral index has been calculated from data within the 14 mm band only to ensure comparability between as many sources as possible. On top of that, detection rates (D-Rate) and the number of epochs when a source was observed with the given receiver are displayed.

| ID<br>(J2000) | $\langle S_{20\text{mm}} \rangle$<br>[Jy] | D-Rate<br>[%] | N <sub>obs</sub> | $\langle S_{14\text{mm}} \rangle$<br>[Jy] | D-Rate<br>[%] | N <sub>obs</sub> | $\langle S_{7\text{mm}} \rangle$<br>[Jy] | D-Rate<br>[%] | N <sub>obs</sub> | $\langle \alpha_{14\text{mm}} \rangle$ |
|---------------|-------------------------------------------|---------------|------------------|-------------------------------------------|---------------|------------------|------------------------------------------|---------------|------------------|----------------------------------------|
| J0035+5950    | 0.0761 ± 0.0094                           | 66            | 6                | 0.0687 ± 0.0052                           | 83            | 12               | -                                        | 0             | 4                | -0.12 ± 0.59                           |
| J0112+2244    | -                                         | -             | 0                | 1.38 ± 0.4                                | 100           | 25               | 1.49 ± 0.46                              | 100           | 24               | 0.28 ± 0.18                            |
| J0136+3906    | 0.041 ± 0.004                             | 100           | 1                | 0.0397 ± 0.0022                           | 100           | 1                | -                                        | -             | 0                | -                                      |
| J0152+0146    | -                                         | 0             | 2                | -                                         | -             | 0                | -                                        | -             | 0                | -                                      |
| J0214+5144    | 0.168 ± 0.017                             | 80            | 5                | 0.151 ± 0.019                             | 78            | 14               | 0.162 ± 0.014                            | 12            | 8                | -0.43 ± 0.25                           |
| J0221+3556    | -                                         | -             | 0                | 0.642 ± 0.024                             | 88            | 9                | 0.5 ± 0.063                              | 100           | 9                | -0.41 ± 0.18                           |
| J0222+4302    | -                                         | -             | 0                | 1.025 ± 0.055                             | 100           | 18               | 0.955 ± 0.077                            | 76            | 17               | -0.09 ± 0.26                           |
| J0232+2017    | 0.0391 ± 0.0041                           | 81            | 11               | 0.042 ± 0.018                             | 56            | 23               | -                                        | 0             | 4                | -0.3 ± 1.4                             |
| J0303-2407    | 0.203 ± 0.016                             | 87            | 8                | 0.187 ± 0.024                             | 87            | 16               | -                                        | 0             | 7                | -0.26 ± 0.56                           |
| J0316+4119    | 0.1405 ± 0.0056                           | 83            | 6                | 0.136 ± 0.013                             | 80            | 20               | -                                        | 0             | 12               | -0.13 ± 0.3                            |
| J0319+1845    | 0.0202 ± 0.0021                           | 50            | 2                | -                                         | 0             | 1                | -                                        | -             | 0                | -                                      |
| J0416+0105    | 0.0565 ± 0.0096                           | 88            | 9                | 0.051 ± 0.011                             | 75            | 16               | -                                        | 0             | 6                | -0.13 ± 0.57                           |
| J0507+6737    | 0.0278 ± 0.0013                           | 25            | 4                | 0.0277 ± 0.0016                           | 22            | 9                | -                                        | 0             | 2                | -                                      |
| J0509+0541    | -                                         | -             | 0                | 1.49 ± 0.44                               | 96            | 27               | 1.32 ± 0.45                              | 84            | 26               | -0.05 ± 0.26                           |
| J0521+2112    | -                                         | -             | 0                | 0.379 ± 0.025                             | 95            | 20               | 0.383 ± 0.037                            | 72            | 18               | 0.01 ± 0.39                            |
| J0648+1516    | 0.0324 ± 0.0064                           | 100           | 1                | 0.0312 ± 0.0024                           | 100           | 1                | -                                        | -             | 0                | -                                      |
| J0650+2502    | 0.0986 ± 0.0038                           | 66            | 6                | 0.0898 ± 0.0077                           | 91            | 12               | -                                        | 0             | 4                | 0.01 ± 0.35                            |
| J0710+5909    | -                                         | 0             | 2                | 0.0452 ± 0.0022                           | 100           | 1                | -                                        | -             | 0                | -                                      |
| J0733+5153    | 0.0752 ± 0.0047                           | 100           | 1                | -                                         | -             | 0                | -                                        | -             | 0                | -                                      |
| J0809+5219    | 0.145 ± 0.01                              | 50            | 2                | 0.116 ± 0.017                             | 100           | 2                | -                                        | 0             | 1                | 0.11 ± 0.14                            |
| J0812+0237    | 0.0362 ± 0.0034                           | 66            | 6                | 0.047 ± 0.012                             | 40            | 5                | -                                        | -             | 0                | -                                      |
| J0847+1135    | -                                         | -             | 0                | -                                         | -             | 0                | -                                        | -             | 0                | -                                      |
| J0913-2103    | 0.1457 ± 0.0068                           | 60            | 5                | 0.1216 ± 0.003                            | 75            | 4                | -                                        | -             | 0                | -0.05 ± 0.67                           |
| J1015+4926    | 0.235 ± 0.017                             | 80            | 5                | 0.221 ± 0.015                             | 92            | 13               | 0.215 ± 0.041                            | 33            | 6                | -0.34 ± 0.37                           |
| J1058+2817    | 0.0909 ± 0.006                            | 85            | 7                | 0.0952 ± 0.0071                           | 87            | 8                | -                                        | 0             | 1                | -0.09 ± 0.39                           |
| J1104+3812    | 0.447 ± 0.0061                            | 100           | 2                | 0.415 ± 0.046                             | 94            | 34               | 0.411 ± 0.061                            | 69            | 29               | -0.06 ± 0.23                           |
| J1136+7009    | 0.164 ± 0.01                              | 80            | 5                | 0.148 ± 0.013                             | 86            | 15               | -                                        | 0             | 7                | -0.19 ± 0.24                           |
| J1136+6737    | 0.0344 ± 0.0026                           | 100           | 1                | -                                         | 0             | 1                | -                                        | -             | 0                | -                                      |
| J1145+1936    | 0.507 ± 0.032                             | 100           | 7                | 0.343 ± 0.02                              | 93            | 15               | 0.224 ± 0.011                            | 28            | 7                | -0.78 ± 0.16                           |
| J1217+3007    | 0.391 ± 0.056                             | 100           | 1                | 0.395 ± 0.054                             | 95            | 21               | 0.404 ± 0.066                            | 89            | 19               | -0.11 ± 0.25                           |
| J1221+3010    | 0.0577 ± 0.0034                           | 85            | 7                | 0.065 ± 0.016                             | 81            | 11               | -                                        | 0             | 2                | -0.03 ± 0.78                           |
| J1221+2813    | 0.521 ± 0.052                             | 50            | 2                | 0.51 ± 0.053                              | 96            | 26               | 0.478 ± 0.064                            | 73            | 23               | -0.17 ± 0.25                           |
| J1224+2436    | 0.038 ± 0.002                             | 100           | 1                | -                                         | -             | 0                | -                                        | -             | 0                | -                                      |
| J1230+2518    | -                                         | -             | 0                | 0.361 ± 0.066                             | 94            | 18               | 0.39 ± 0.11                              | 86            | 15               | -0.06 ± 0.36                           |
| J1415+1320    | 0.6724 ± 0.0029                           | 100           | 1                | 0.639 ± 0.018                             | 100           | 3                | 0.7071 ± 0.0074                          | 100           | 2                | -0.15 ± 0.21                           |
| J1422+3223    | 0.675 ± 0.023                             | 100           | 2                | 0.8 ± 0.16                                | 92            | 27               | 0.88 ± 0.22                              | 88            | 25               | 0.24 ± 0.25                            |
| J1427+2348    | 0.416 ± 0.042                             | 100           | 1                | 0.391 ± 0.03                              | 100           | 22               | 0.381 ± 0.048                            | 60            | 20               | -0.11 ± 0.22                           |
| J1428+4240    | 0.0304 ± 0.0046                           | 33            | 6                | 0.0225 ± 0.0021                           | 7             | 14               | -                                        | 0             | 2                | -                                      |
| J1443+1200    | 0.0385 ± 0.0025                           | 50            | 2                | 0.0417 ± 0.006                            | 100           | 1                | -                                        | -             | 0                | -                                      |
| J1443+2501    | 0.224 ± 0.029                             | 78            | 14               | 0.189 ± 0.029                             | 100           | 20               | -                                        | 0             | 4                | -0.26 ± 0.26                           |
| J1518-2731    | 0.235 ± 0.043                             | 66            | 3                | 0.207 ± 0.023                             | 71            | 7                | -                                        | 0             | 3                | -0.45 ± 0.57                           |
| J1555+1111    | 0.346 ± 0.03                              | 91            | 12               | 0.316 ± 0.036                             | 96            | 27               | 0.301 ± 0.056                            | 50            | 12               | -0.08 ± 0.24                           |
| J1653+3945    | 1.178 ± 0.043                             | 100           | 2                | 1.031 ± 0.027                             | 100           | 24               | 0.884 ± 0.071                            | 81            | 21               | -0.2 ± 0.13                            |
| J1725+1152    | 0.0995 ± 0.0074                           | 100           | 1                | 0.0949 ± 0.0028                           | 100           | 1                | -                                        | -             | 0                | -                                      |
| J1728+5013    | 0.1226 ± 0.0069                           | 77            | 9                | 0.122 ± 0.01                              | 95            | 22               | -                                        | 0             | 11               | -0.17 ± 0.38                           |
| J1743+1935    | 0.2194 ± 0.0087                           | 77            | 9                | 0.194 ± 0.016                             | 100           | 22               | -                                        | 0             | 11               | -0.19 ± 0.33                           |
| J1813+3144    | 0.1169 ± 0.004                            | 75            | 8                | 0.1111 ± 0.0067                           | 100           | 17               | -                                        | 0             | 4                | -0.19 ± 0.46                           |
| J1943+2118    | 0.0358 ± 0.0064                           | 66            | 6                | 0.0316 ± 0.0022                           | 14            | 7                | -                                        | -             | 0                | -                                      |
| J1958-3011    | 0.07635 ± 0.00049                         | 66            | 3                | 0.1 ± 0.014                               | 33            | 3                | -                                        | -             | 0                | -                                      |
| J1959+6508    | 0.213 ± 0.023                             | 100           | 8                | 0.204 ± 0.018                             | 78            | 23               | 0.212 ± 0.011                            | 18            | 11               | 0.04 ± 0.31                            |
| J2001+4352    | 0.311 ± 0.081                             | 100           | 2                | 0.3 ± 0.052                               | 100           | 2                | -                                        | -             | 0                | -0.3814 ± 0.0031                       |
| J2039+5219    | 0.0285 ± 0.0039                           | 100           | 1                | -                                         | 0             | 1                | -                                        | -             | 0                | -                                      |
| J2158-3013    | 0.342 ± 0.022                             | 60            | 5                | 0.334 ± 0.06                              | 63            | 11               | -                                        | 0             | 6                | -0.54 ± 0.28                           |
| J2250+3825    | -                                         | 0             | 2                | -                                         | -             | 0                | -                                        | -             | 0                | -                                      |
| J2243+2021    | 0.099 ± 0.01                              | 40            | 10               | 0.0981 ± 0.0087                           | 77            | 9                | -                                        | -             | 0                | 0.3 ± 0.28                             |
| J2347+5142    | 0.1623 ± 0.0086                           | 83            | 6                | 0.154 ± 0.011                             | 84            | 19               | -                                        | 0             | 12               | -0.33 ± 0.33                           |

only one sub-frequency detected, this is vastly different, since no sensible fits can be performed. As stated earlier, the best value is therefore calculated by assuming a flat spectrum ( $\alpha=0$ ). The uncertainty of this value is estimated in a similar manner to the min/max-fits mentioned earlier. Again, the measurement uncer-

tainties are subtracted/added to the flux density value. Then, different spectral distributions with  $\alpha \in \{-0.5; 0; 0.5\}$ , originating at the min/max flux densities, are considered. This means, one gets three alternate spectral distributions for max and min flux density, respectively. Analogous to the previous calculations, the



difference between the integrated alternate spectral distributions and the integrated best fit (in this case the flat spectrum) is calculated. The maximum difference is then used as the average flux density error.

In the following sections, when referring to flux densities at 7 mm, 14 mm or 20 mm, we always refer to the sub-band-averaged flux density in each band, calculated using the method introduced in this section if not declared otherwise.

### 3.2.2. Flux Densities in the TELAMON sample

The sub-band averaging procedure introduced in the previous section provides us with one flux density value at 20 mm, 14 mm and 7 mm for every source at every epoch in case it was observed and detected. In order to get an overview of the general source properties we calculate the average flux densities of every source for 20 mm, 14 mm and 7 mm over time from the sub-band averaged flux densities. This allows us to characterize the observed sample in terms of average source flux density. All average flux density values are presented in Table 3. The errors hereby correspond to the standard deviation of the sub-band averaged flux densities. In the special case where a source has only been detected once, the presented uncertainty is equal to the error of the sub-band averaged flux density. All average flux densities presented in Table 3 are also depicted as histogram plots in Fig. 6 binned according to the source types. Here one can see that the 7 mm flux densities (Fig. 6, bottom) are by far the smallest sample and limited to flux densities  $\geq 150$  mJy. Only 18 out of 37 observed sources show a significant detection at 7 mm. This can be explained by the detection limit of the 7 mm receiver (see Sect. 4.3) and by the fact that most of the sources in our sample are too faint to be detectable at 7 mm. This is vastly different at 20 mm and 14 mm. At 14 mm (Fig. 6, center), 48 of the 51 observed sources show a significant detection in at least one epoch. At 20 mm (Fig. 6, top), 46 of the 49 observed sources show a significant detection in at least one epoch.

Following from the values presented in Table 3, we find an average source flux density of 0.57 Jy with a standard deviation of 0.39 Jy and a median of 0.41 Jy in our sample. This can only be considered as an upper limit to the average flux density of the entire sample presented in Table 1, since it is heavily biased by the non-detection of sources with flux densities  $\leq 150$  mJy due to the sensitivity limit at 7 mm. At 14 mm the average source flux density is 0.29 Jy with a standard deviation of 0.34 Jy and a median of 0.15 Jy. At 20 mm we find an average source flux density of 0.21 Jy with a standard deviation of 0.23 Jy and a median of 0.13. At the latter two wavelengths, the receiver sensitivity also limits the detection of very faint sources, but since almost all sources from our sample were detected in these bands we consider this bias to be much less significant than for 7 mm. This allows us to perform a sensible statistical comparison of the 20 mm and 14 mm data. For both wavelengths we find that according to a two sample KS-test one has to reject the null-hypothesis that XBL and HBL have the same underlying statistical distribution with high significance. This also becomes clear when looking at the top and center histogram plots in Fig. 6. The sub-sample of XBLs seems to populate much lower average flux densities than the sub-sample of HBLs. Moreover, the median average flux densities support this finding: at 20 mm the subsample of XBLs exhibits a median average flux density of 0.076 Jy while for HBLs one finds a median of 0.24 Jy. At 14 mm the subsample of XBLs exhibits a median average flux density of 0.095 Jy while for HBLs one finds a median of 0.27 Jy. In summary, the sub-sample of HBLs shows higher flux densities than the sub-

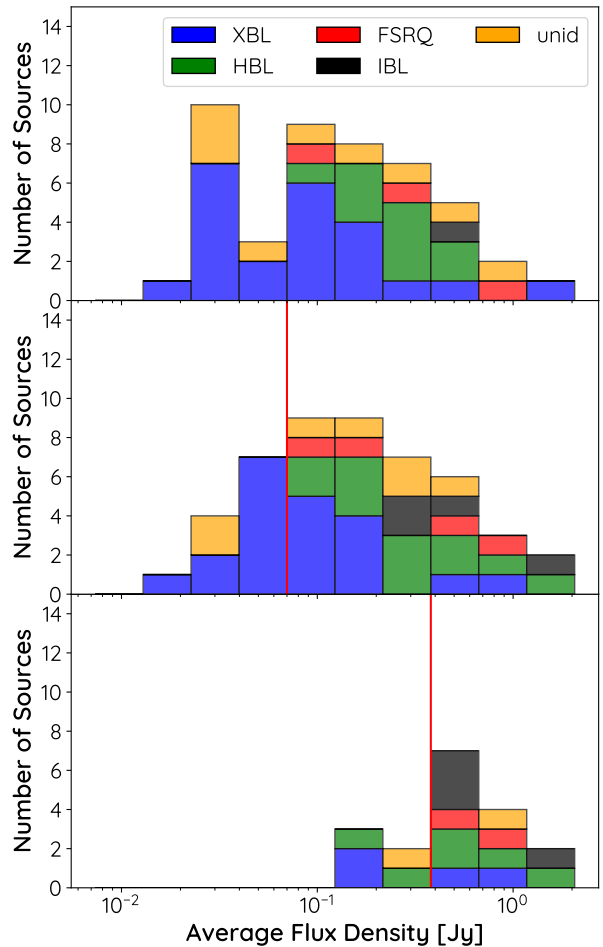


**Fig. 6.** Distribution of the average flux density found in the TELAMON sample sources for the 20 mm (top), 14 mm (center), and 7 mm (bottom) receivers.

sample of XBLs in both bands. This is consistent with the per definition higher synchrotron peak frequencies of XBLs and the blazar sequence (Fossati et al. 1998; Donato et al. 2001) which suggests that sources become fainter in the radio band with increasing synchrotron peak frequency.

### 3.3. Detection Rates

In order to analyze the impact of the receiver sensitivity on the detectable source flux density, we calculate detection rates for all observed sources and receivers. For every source we count the observing epochs (dates) during which the source was observed and the epochs where the source was detected in at least one sub-frequency of the given receiver. The detection rate is then given by the number of detections divided by the number of observations. The detection rates and number of observations for all receivers and sources are presented in Table 3 next to the average flux density values.

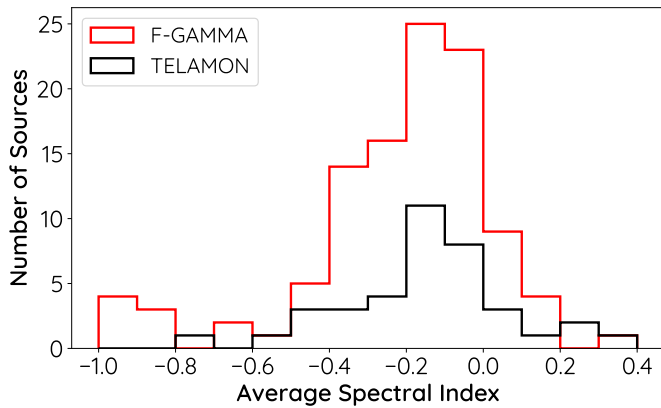


**Fig. 7.** Histogram plot of average spectral indices for all sources from the F-GAMMA (red) sample (Angelakis et al. 2019) and the TELAMON (black) sample. Both distributions cannot be distinguished from each other.

## 4. Discussion

In this section we will discuss and compare the TELAMON source properties with previous programs, namely the F-GAMMA monitoring (Fuhrmann et al. 2016; Liodakis et al. 2017; Angelakis et al. 2019) and a study on TeV-selected blazars by Lindfors et al. (2016).

### 4.1. Spectral Index Discussion

Since the study by Lindfors et al. (2016) was carried out only at a single radio frequency (15 GHz) we can only compare spectral indices with the F-GAMMA program. Angelakis et al. (2019) provide spectral indices for various frequency windows, however, none of them is comparable with the TELAMON spectral range (i.e., 15 GHz–44 GHz). We have therefore used light curves provided by Angelakis et al. (2019) to derive spectral indices similar to Sec. 3.1.1 only taking into account flux density values for frequencies 14.6 GHz, 23.05 GHz and 32 GHz to ensure comparability between the derived spectral indices for TELAMON and F-GAMMA. Fig. 7 shows a direct comparison of the distribution of both samples in form of a histogram plot. The overall sample size of F-GAMMA is superior to the TELAMON sample but both distributions look very similar. Indeed, a two-sample KS-test leads to a p-value of  $p = 0.81$  which clearly indicates that the distributions cannot be distinguished and most likely have the same underlying statistics. Note that the F-GAMMA sample includes several sources with a steep spectrum ( $\alpha \lesssim 0.8$ ) which the TELAMON sample does not show. Those are mostly calibrator sources which we did not exclude in our analysis of F-GAMMA data. We can therefore follow that the spectral index distribution of the GeV-selected F-GAMMA sample and the TeV-detected TELAMON sample cannot be distinguished from each other.

### 4.2. Flux Density Discussion

Similar to the spectral index comparison, we have calculated average flux densities for the F-GAMMA data at 23.05 GHz from Angelakis et al. (2019) to compare with the TELAMON sample. On top of that, we use the average flux density values provided by Lindfors et al. (2016) to compare with the TELAMON sources. All three flux density distributions are depicted in Fig. 8. One can clearly see that the flux densities of the GeV-selected F-

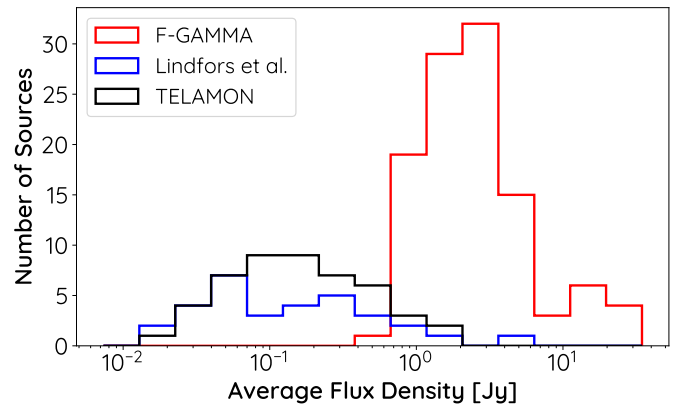


**Fig. 8.** Comparison of the F-GAMMA (Angelakis et al. 2019), Lindfors et al. (2016) and TELAMON samples according to the average source flux density.

GAMMA sources are in general much higher than for the TeV-selected Lindfors et al. (2016) and TELAMON samples. This is consistent with the fact that most TeV emitting blazars have their SED shifted to higher energies and are consequently fainter in the radio band. We further performed a two-sample KS-test to compare TELAMON flux densities with the F-GAMMA and Lindfors et al. (2016) sample and find with very high significance that the TELAMON and Lindfors et al. (2016) sources show a similar distribution while we have to neglect the null-hypothesis of similar underlying distributions for TELAMON and F-GAMMA. We therefore conclude that this difference in flux density seems to be characteristic for the target selection of either GeV- (F-GAMMA) or TeV-selected (TELAMON, Lindfors et al. (2016)) blazars.

### 4.3. A Long-term Monitoring Strategy

In order to find a TeV-blazar sample well suited for long-term monitoring observations with the Effelsberg 100-m telescope, we discuss the relationship between source flux density and detection rate for all three receivers (20 mm, 14 mm and 7 mm) in this section. This is important since one can see in Table 3 that for some very faint sources the detection rate is rather low (i.e.,  $\sim 10\%$ ). Observing these kind of sources in a long-term monitoring study would lead to a lot of telescope time wasted that could be used to include other (brighter) sources with better detection potential. On top of that, in order to perform variability and multi-wavelength correlation studies, a sufficient sample size (flux density measurements per source) are required, which would take decades for sources with such low detection rates and the current cadence of 2 to 4 weeks. We therefore require a detection rate above 50% (i.e., a source detection at least every other epoch) to optimize the scientific outcome of the observing time and to prevent too many non-detections in the context of a future long-term monitoring setup.

In principle, the detection rate should only depend on the sensitivity of the receiver and can be calculated by telescope intrinsic parameters. However, for a long-term monitoring program, also bad weather epochs can influence the detectability of fainter sources, especially at the highest frequencies. We consider the here presented 1.5 year observations to be a good representation of such effects and therefore well suited to identify a flux density limit above which it is sensible to monitor sources in form of a long-term study with the given telescope and receiver

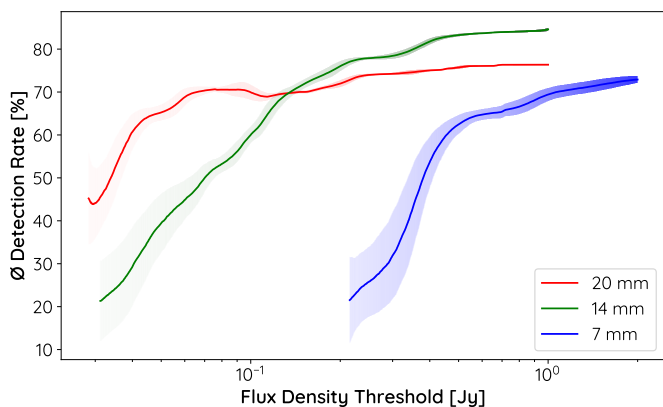


**Fig. 9.** Average detection rate for sources below a given flux density threshold for the 20 mm, 14 mm and 7 mm receiver as calculated from the first 1.5 years of TELAMON observations.

setup. For each receiver, we calculate the average detection rate for all sources below a certain flux density threshold. This is done for 10,000 different flux density thresholds. Moreover, this entire procedure is carried out 1,000 times with varying average source flux densities in a Monte-Carlo (MC) way, assuming the average flux densities and their error in Table 3 correspond to Gaussian distributions. The mean average detection rate and its standard deviation taken from the 1,000 MC-iterations is then plotted in Fig. 9 for 10,000 different flux density threshold values. In order to guarantee statistical convergence, we require a minimum of three sources to be included in the average detection rate count, therefore the average detection rates in Fig. 9 can only be presented above a certain flux density threshold. If we assume, that the detection rate is monotonically increasing with flux density, the detection rate curves in Fig. 9 correspond to lower limits of the actual detection rate at any given flux density. This analysis is therefore well suited to find one flux density limit  $S_0$  for each receiver above which we expect a detection rate of at least 50%. For the 20 mm receiver this is at  $S_0 = 33.8^{+3.1}_{-5.3}$  mJy, for the 14 mm receiver we find  $S_0 = 70.2^{+5.8}_{-8.3}$  mJy and for 7 mm  $S_0 = 380^{+29}_{-44}$  mJy.

Sources below a 20 mm flux density of  $\sim 34$  mJy do not have a sufficient detection chance with either of the three introduced receivers. We therefore suggest to observe these sources at even longer wavelengths (e.g. 45 mm at Effelsberg) to have best chances to detect them in a long-term monitoring program. The second faintest sources, exhibiting a 20 mm flux density  $\gtrsim 34$  mJy but a 14 mm flux density 70 mJy should only be monitored at 20 mm in the current observing setup. Brighter sources ( $S_{14\text{mm}} \gtrsim 70$  mJy and  $S_{7\text{mm}} \lesssim 380$  mJy) can be monitored at 20 mm and 14 mm in a sensible way and for the brightest sources ( $S_{7\text{mm}} \gtrsim 380$  mJy) one could go down to wavelengths of 14 mm and 7 mm for sensible monitoring. Note that in principle these thresholds can be improved by spending more time on each source, however this is not favorable since one needs to find an ideal trade-off between observing time spend per source and the total number of sources that can be monitored. The here suggested four different sub-samples and flux-density thresholds are an almost ideal setup for this kind of observation with the Effelsberg telescope and will be implemented for future TELAMON observations.

## 5. Conclusions & Outlook

We have presented the first results of the pilot-phase of the TELAMON AGN monitoring program for a complete sample of TeV-emitting blazars.

Our results are consistent with the findings of a prior study of the same object class by Lindfors et al. (2016). In comparison to the GeV-selected F-GAMMA sample Fuhrmann et al. (2016); Angelakis et al. (2019) we find that the spectral indices of both, GeV- and TeV-selected sources are consistent with a flat spectrum. The average flux density at 14 mm is significantly lower in our TeV-selected sample than what Angelakis et al. (2019) have found in their study.

In future studies we will address questions, such as the variability of TeV-blazars and correlation studies with multi-wavelength lightcurves. Moreover, the TELAMON program will continue its observations using an optimized observing setup as proposed in this paper. In the future, the TELAMON team will not only provide important results on the monitored TeV-sample but also on the performed neutrino-candidate follow-up observations which have not been discussed in this paper. On top of that, we are currently working on deriving polarization for all observed sources.

*Acknowledgements.* Part of this work was supported by the German *Deutsche Forschungsgemeinschaft*, DFG project number XXXX. This work is based on observations with the Effelsberg 100-m telescope.

## References

- Abazajian, K. N., Adelman-McCarthy, J. K., Agüeros, M. A., et al. 2009, *ApJS*, 182, 543
- Ackermann, M., Ajello, M., Atwood, W. B., et al. 2015, *ApJ*, 810, 14
- Ahn, C. P., Alexandroff, R., Allende Prieto, C., et al. 2012, *ApJS*, 203, 21
- Ahnen, M. L., Ansoldi, S., Antonelli, L. A., et al. 2017, *A&A*, 603, A25
- Angelakis, E., Fuhrmann, L., Myserlis, G., et al. 2019, *A&A*, 626, A60
- Baars, J. W. M., Genzel, R., Pauliny-Toth, I. I. K., & Witzel, A. 1977, *A&A*, 500, 135
- Biteau, J., Prandini, E., Costamante, L., et al. 2020, *Nature Astronomy*, 4, 124
- Chang, Y. L., Arsioli, B., Giommi, P., Padovani, P., & Brandt, C. H. 2019, *A&A*, 632, A77
- Chou, Y.-I. 1975, *Statistical Analysis* (Holt, Rinehart & Winston of Canada Ltd.)
- Ciprini, S., Tosti, G., Teräsranta, H., & Aller, H. D. 2004, *MNRAS*, 348, 1379
- Donato, D., Ghisellini, G., Tagliaferri, G., & Fossati, G. 2001, *A&A*, 375, 739
- Fossati, G., Maraschi, L., Celotti, A., Comastri, A., & Ghisellini, G. 1998, *MNRAS*, 299, 433
- Fuhrmann, L., Angelakis, E., Zensus, J. A., et al. 2016, *A&A*, 596, A45
- Ghisellini, G. 1999, *Astroparticle Physics*, 11, 11, *TeV Astrophysics of Extragalactic Sources*
- Giommi, P., Glauch, T., Padovani, P., et al. 2020, *MNRAS*, 497, 865
- Hachisuka, K., Brunthaler, A., Menten, K. M., et al. 2006, *ApJ*, 645, 337
- Hillas, A. M. 1984, *ARA&A*, 22, 425
- Lindfors, E. J., Hovatta, T., Nilsson, K., et al. 2016, *A&A*, 593, A98
- Liodakis, I., Marchili, N., Angelakis, E., et al. 2017, *MNRAS*, 466, 4625
- Mannheim, K. 1995, *Astroparticle Physics*, 3, 295
- Moré, J. J. 1978, in *Numerical Analysis*, ed. G. A. Watson (Berlin, Heidelberg: Springer Berlin Heidelberg), 105–116
- Nieppola, E., Tornikoski, M., & Valtaoja, E. 2006, *A&A*, 445, 441
- Ott, M., Witzel, A., Quirrenbach, A., et al. 1994, *A&A*, 284, 331
- Padovani, P. & Giommi, P. 1995, *ApJ*, 444, 567
- Padovani, P., Petropoulou, M., Giommi, P., & Resconi, E. 2015, *MNRAS*, 452, 1877
- Paiano, S., Landoni, M., Falomo, R., et al. 2017, *ApJ*, 837, 144
- Perley, R. A. & Butler, B. J. 2013, *ApJS*, 204, 19
- Perley, R. A. & Butler, B. J. 2017, *ApJS*, 230, 7
- Shaw, M. S., Romani, R. W., Cotter, G., et al. 2012, *ApJ*, 748, 49
- Shaw, M. S., Romani, R. W., Cotter, G., et al. 2013, *ApJ*, 764, 135
- Sowards-Emmerd, D., Romani, R. W., Michelson, P. F., Healey, S. E., & Nolan, P. L. 2005, *ApJ*, 626, 95
- Tavecchio, F., Ghisellini, G., & Guetta, D. 2014, *ApJ*, 793, L18
- Zijlstra, A. A., van Hoof, P. A. M., & Perley, R. A. 2008, *ApJ*, 681, 1296